Journal of Materials Research and Technology 38 (2025) 4953–4964

Contents lists available at ScienceDirect

Journal of Materials Research and Technology

journal homepage: www.elsevier.com/locate/jmrt

Understanding the limited protectiveness of Si-rich passive film on Fe-based shape memory stainless steels in highly oxidizing media

R. Silva [a,b,c,*], G.S. Vacchi [a], J.G.C. Passos [a], P. Hammer [d], J.A.C.P. Gomes [c], C.A.D. Rovere [a,b,**]

[a] Munir Rachid Corrosion Laboratory, Department of Materials Engineering, Federal University of São Carlos, Rodovia Washington Luis Km 235, 13565-905, São Carlos, SP, Brazil
[b] Federal University of São Carlos, Graduate Program in Materials Science and Engineering, Brazil
[c] Corrosion Laboratory, Material and Metallurgical Engineering Program, COPPE, Federal University of Rio de Janeiro, Technology Center, Rio de Janeiro, RJ, Brazil
[d] Institute of Chemistry, São Paulo State University, Araraquara, 14800-900, SP, Brazil

ARTICLE INFO

Keywords:
Fe–Mn–Si–Cr–Ni-(Co) shape memory stainless steels
Electrochemical corrosion
Passive film
EIS
Potentiodynamic polarization
XPS

ABSTRACT

Fe–Mn–Si–Cr–Ni-(Co) shape memory stainless steels (SMSSs) are smart, low-cost materials that offer good mechanical properties and corrosion resistance and are suitable for use in oxidizing environments due to their elevated Si content, which helps suppress intergranular corrosion commonly observed in conventional austenitic stainless steels such as 304L, under oxidizing conditions. However, their corrosion resistance in highly oxidizing media, such as those found in spent fuel reprocessing, is not yet fully understood. This study investigates two SMSS formulations and compares their electrochemical corrosion and passive film characteristics with SS 304L in 6 M and 11.5 M HNO_3 solutions, relevant for nuclear fuel reprocessing. All alloys exhibited spontaneous passivation, with stable passive films formed on SS 304L and SMSS B, while film stability on SMSS A decreased with increasing HNO_3 concentration. Despite their lower Cr content, the SMSSs exhibited good passivation and slightly higher transpassive breakdown potentials than SS 304L, which suffered from intergranular corrosion. In contrast, the SMSSs exhibited generalized corrosion. The high protection of the passive films formed on the SMSSs is mainly attributed to their high Si content (72–85 at.%) in the form of SiO_2, highlighting their potential, especially SMSS B, for applications in highly oxidizing environments. The findings show that although Si improves corrosion resistance in oxidizing media, its protective effect is limited in the absence of Cr. A synergistic combination of Si and Cr in the passive film is essential to ensure the stability of the oxide layer under aggressive conditions.

1. Introduction

Nuclear fuel reprocessing is a chemical process used to extract fission products and recover unreacted material, thereby improving fuel efficiency and reducing waste volume [1,2]. The process involves dissolving spent fuel in concentrated nitric acid at high temperatures, creating a highly oxidizing medium. The presence of species such as Ru^{7+}, Pu^{6+} and Ce^{4+} from the fuel, as well as Cr^{6+} ions released from stainless steel components, increases the corrosive nature of the environment and compromises the durability of structural materials [2–6]. To withstand such aggressive conditions, austenitic stainless steels are widely employed due to their ability to form thin, protective Cr-rich passive films that ensure high corrosion resistance in nitric acid environments [4,6,7]. However, structural materials must also exhibit resistance to transpassive corrosion, intergranular corrosion (IGC) and generalized corrosion, considering variations in acid concentration, temperature, and the presence of oxidizing species. Commonly used grades include low-carbon 304L (SS 304 L), stabilized types such as 310Nb, 321Ti and 347Nb [4,8,9].

Despite the use of corrosion-resistant austenitic grades, conventional

* Corresponding author. Munir Rachid Corrosion Laboratory, Department of Materials Engineering, Federal University of São Carlos, Rodovia Washington Luis Km 235, 13565-905, São Carlos, SP, Brazil.
** Corresponding author. Munir Rachid Corrosion Laboratory, Department of Materials Engineering, Federal University of São Carlos, Rodovia Washington Luis Km 235, 13565-905, São Carlos, SP, Brazil.
E-mail addresses: rsilva@ufscar.br (R. Silva), rovere@ufscar.br (C.A.D. Rovere).

https://doi.org/10.1016/j.jmrt.2025.08.222
Received 5 May 2025; Received in revised form 15 August 2025; Accepted 25 August 2025
Available online 28 August 2025

SS 304L can undergo transpassive corrosion and severe IGC in highly oxidizing nitric acid environments, particularly in the presence of oxidizing species at elevated temperatures, resulting in unacceptably high corrosion rates and compromising the structural integrity of critical components in reprocessing plants [4,10–13]. Under such conditions, the corrosion potential (E_{corr}) can shift into the transpassive region, promoting preferential dissolution along grain boundaries [2,8]. These degradation processes can occur even in the absence of Cr-rich carbides (non-sensitized condition) and are mainly related to grain boundary structure and electrochemical activity, which are influenced by the localized enrichment of impurity elements such as phosphorus (P), sulfur (S), silicon (Si), and boron (B) [2,4,14]. To improve the resistance of stainless steel to IGC in oxidizing nitric acid environments, high-purity refining is commonly used to minimize impurity levels [2,8]. While this process mitigates IGC susceptibility, additional strategies are needed to fully address the challenges posed by spent fuel reprocessing conditions.

One such approach is alloy modification, particularly the addition of high Si content to low-C stainless steels, which has been shown to significantly improve their IGC resistance in HNO_3 solutions when about 4–5 wt.% Si is added [4,8,9,15]. As reported in the literature [9,15–17], the effect of Si on IGC of stainless steels in nitric acid depends on its concentration. At levels below ~1 wt%, Si tends to accelerate IGC, while concentrations above 1.5 wt% progressively improve resistance. Complete mitigation of IGC has been observed at Si contents of 5 wt% [16]. However, the IGC resistance of Si-containing stainless steels is not only influenced by its content, but also by its distribution within the microstructure - whether it is segregated at grain boundaries, dissolved in the γ-phase, or present as secondary phases. In addition, the composition and operating conditions of the corrosive environment play a significant role in determining the overall performance of the material [9,18].

While the benefits of Si in improving the IGC resistance of stainless steels in oxidizing nitric acid environments are well documented, the underlying mechanism remains under debate. Several explanations have been proposed to clarify this effect. One hypothesis is that Si hinders the precipitation of Cr-rich carbides, preventing the development of Cr-depleted zones near grain boundaries, which are particularly prone to selective dissolution [2,18]. Another explanation is that Si influences the stability of grain boundaries, reducing their energy and limiting potential gradients, thereby decreasing their susceptibility to IGC [19]. In addition, Si has been reported to promote the formation of a protective Si-rich oxide film, which contributes significantly to improved corrosion resistance [6]. Despite these findings, further studies are needed to fully elucidate the dominant mechanism responsible for the improved IGC resistance of Si-containing stainless steels.

Given the significant role of Si in improving the transpassive intergranular corrosion resistance of stainless steels in HNO_3 solutions, it is of interest to explore alternative alloying strategies that take advantage of this element. In this context, previous investigations in our laboratory [20–22] have shown that Fe–Mn–Si–Cr–Ni-(Co) shape memory stainless steels (SMSSs) can form highly stable passive films when polarized at elevated anodic potentials in sulfuric acid solutions, indicating their potential for use in highly oxidizing media. This behavior has been attributed primarily to the enrichment of Si in the passive layer, which contributes to enhanced film stability under such conditions. Interestingly, in addition to the corrosion resistance provided by Si, these alloys also exhibit the shape memory effect (SME), which distinguishes them from conventional stainless steels. Beyond the SME, these alloys also offer practical advantages such as low production costs, excellent machinability, good weldability, mechanical properties and corrosion resistance [21,23,24].

In these ferrous alloys, SME is associated with stress-induced martensitic transformation (γ → ε) and its reversal upon heating [25–27]. This unique property makes them a promising alternative for improving the functionality and durability of assembled structures in various industries. For example, Fe–Mn–Si–Cr–Ni-(Co) SMSSs offer a cost-effective solution for joining pipe sections without welding [28]. This approach eliminates the formation of heat-affected zones (HAZ), which are prone to sensitization and intergranular corrosion in highly oxidizing environments such as spent fuel reprocessing systems. By avoiding these issues, SME-assisted coupling improves both mechanical integrity and corrosion resistance in critical applications. However, understanding their corrosion resistance in highly oxidizing media, particularly those typical of spent fuel reprocessing, remains essential to assessing their applicability.

Therefore, this work aims to evaluate the electrochemical corrosion behavior of two Fe–Mn–Si–Cr–Ni-(Co) SMSSs in concentrated HNO_3 solutions by characterizing the passive film formed on these Fe-based shape memory alloys, which have a considerable amount of Si (about 5 wt%) but low Cr content (<13 wt%) when compared to a conventional austenitic stainless steel (~18 wt%). This study builds upon an earlier investigation by our group [29], which indicated that the high Si content in a Fe–Mn–Si–Cr–Ni-(Co) SMSS contributed to enhanced corrosion resistance. However, this study was limited to a single alloy composition and test condition (11.5 M HNO_3) and did not include comprehensive electrochemical or surface characterization. The present work takes a more systematic approach by examining two distinct SMSS compositions exposed to varying concentrations of nitric acid, combining electrochemical techniques with boiling immersion tests. The results provide a deeper understanding of the influence of alloying elements on the composition and electrochemical properties of the passive films and are directly compared to the passive layer formed on conventional SS 304L.

2. Experimental procedure

2.1. Material and sample characterization

Fe–Mn–Si–Cr–Ni-(Co) SMSSs were melted in a vacuum induction furnace (VIM) using high-purity Fe, Mn, Si, Cr, Ni, and Co, followed by hot forging at 1280 °C into a bar shape, solution treatment at 1050 °C for 1 h, and quenching in a water bath at room temperature (25 °C). Cylindrical samples (Ø 6.0 mm × 8.0 mm) were then cut by electric discharge machining (EDM) for microstructural characterization, electrochemical corrosion testing, and passive film analysis. The chemical composition of the SMSSs is shown in Table 1. The SMSSs were designed with distinct Cr and Mn contents and the addition of Co exclusively in SMSS B to evaluate how the Cr/Si ratio influences corrosion resistance and how Mn and Co contents affect phase stability. Carbon (C) content was quantified by pyrolysis using a LECO CS-844 analyzer. All other elements were determined by inductively coupled plasma optical emission spectrometry (ICP-OES). For a comparative analysis of the electrochemical behavior and passive film characterization, commercial SS 304L samples (chemical composition listed in Table 1) were subjected to the same solution treatment at 1050 °C for 1 h followed by quenching in a water bath.

For microstructural characterization, the SMSS samples were embedded in conductive bakelite, followed by successive grinding with SiC paper to 1200-grit and mechanical polishing with a 1.0 μm alumina suspension. To eliminate mechanically induced ε-martensite formed during metallographic preparation, an electrolytic polishing step was performed in a 95 % CH_3COOH and 5 % $HClO_4$ solution at 30 V at room temperature. Phase mapping was performed by electron backscatter

Table 1
Chemical composition (wt.%) of the studied Fe–Mn–Si–Cr–Ni-(Co) SMSSs and SS 304L.

Alloy	Fe	Mn	Si	Cr	Ni	Co	Mo	C
SMSS A	bal.	10.34	5.31	9.92	4.87	–	–	0.006
SMSS B	bal.	8.26	5.25	12.80	5.81	11.84	–	0.009
SS 304 L	bal.	1.76	0.39	19.28	7.64		0.25	0.029

diffraction (EBSD) in a Tescan Mira 3 scanning electron microscope (FEG-SEM) with a data acquisition step size of 0.5 μm. In addition, phase identification was performed by X-ray diffraction (XRD) in a Bruker D8 Advance ECO diffractometer equipped with a Cu Kα radiation source (40 kV, 25 mA), scanning over a 2θ range from 30° to 90° at a rate of 2°/min.

2.2. Electrochemical measurements in 6 M and 11.5 M HNO_3 solutions

For electrochemical measurements, SMSSs and SS 304L samples were connected to copper wires and embedded in polyester resin, leaving a circular surface area of 0.283 cm^2 exposed. The tests were performed in 6 M and 11.5 M HNO_3 solutions using a conventional three-electrode electrochemical cell consisting of a platinum counter electrode, a saturated calomel electrode (SCE) as the reference, and the sample as the working electrode. Measurements were performed using a Gamry Reference 3000 potentiostat, with the solutions naturally aerated at room temperature. For each alloy, the average values from five tests were used.

Prior to each electrochemical measurement, the samples were ground to 600-grit silicon carbide (SiC) paper, washed in distilled water, and immediately immersed in the electrochemical cell. The time of exposure to air between grinding and immersion was minimized and kept consistent across all specimens to reduce the influence of air-formed oxide films. The open circuit potential (OCP) was monitored for a period of 90 min to ensure stabilization before starting the measurements. The EIS measurements were performed by superimposing an AC voltage of 10 mV amplitude relative to the stable OCP in the frequency range from 100 kHz to 10 mHz. Potentiodynamic polarization was performed starting 200 mV below the stabilized OCP with a continuous potential sweep up to 1300 mV_{SCE} at a scan rate of 1 mV/s. The transpassive breakdown potential (E_{TP}) was defined as the potential at which the anodic current density continuously increased above 100 $\mu A/cm^2$ [9]. After the tests, the surface morphology of the samples was analyzed using Axiotech Zeiss optical microscopy (OM) and SEM.

2.3. X-ray photoelectron spectroscopy (XPS) analysis

X-ray photoelectron spectroscopy (XPS) was used to determine the chemical composition of the passive film formed on the alloy surfaces after polarization at +800 mV_{SCE} in 11.5 M HNO_3 solution for 1 h. The analyses were performed using a UNI-SPECS UHV system spectrometer at a base pressure of 10^{-7} Pa. The Mg Kα line ($h\nu = 1253.6$ eV) was used as the excitation source with the analyzer pass energy set to 10 eV. High-resolution spectra of Fe 2p, Cr 2p, Si 2p, and O 1s were processed after subtraction of the inelastic background noise using the Shirley method. Elemental composition was obtained from the relative peak areas using Scofield atomic sensitivity factors with an estimated accuracy of ±5 %. Peak fitting was performed using a Voigt function with Gaussian (70 %) and Lorentzian (30 %) components. The full width at half maximum (FWHM) ranged from 1.2 to 2.2 eV, while peak positions were determined to an accuracy of ±0.1 eV. The chemical states were evaluated by analyzing the photoelectron binding energies in relation to available reference data [18,21,30,31].

2.4. Immersion tests in boiling 11.5 M HNO_3 solution

For the immersion tests, circular SMSS samples (20 mm diameter, 3 mm thickness, with a 2 mm diameter hole for mounting), previously polished with a 1 μm alumina suspension, were placed in 500 mL glass flasks equipped with glass condensers and immersed in boiling 11.5 M HNO_3 solution for a total of 240 h, with the solution renewed every 48 h. At the end of the exposure period, the samples were carefully rinsed with distilled water, cleaned with acetone, and dried with hot air. Weight changes were recorded, with loose corrosion products removed during the cleaning process to ensure accurate measurements. The average corrosion rate was determined from five samples of each alloy. After 240 h of immersion, the surface morphology of the samples was analyzed by SEM. In cases where an oxide layer was present on substrate after the immersion test, its crystallographic structure was analyzed by grazing incidence X-ray diffraction (GIXRD) at an incidence angle of 2°. This method enhances the detection of surface oxides while reducing interference from the substrate.

3. Results and discussion

Fig. 1 shows EBSD phase maps and XRD patterns of SMSSs A and B. SMSS A [Figure (a)] exhibits an austenitic (γ) matrix with a high proportion of martensite-α′ and a small amount of martensite-ε, while SMSS B [Fig. 1 (c)] is predominantly austenitic with dispersed martensite-ε islands. The XRD results confirm these findings, identifying austenite, martensite-α′ and martensite-ε in SMSS A [Fig. 1 (b)], and austenite and martensite-ε in SMSS B [Fig. 1 (d)]. The presence of martensite-α′ in SMSS A can be attributed to the lower Mn content compared to that of conventional Fe–14Mn–5Si–9Cr–5Ni [32], which favors the transformation of austenite to martensite-α′, acting as a barrier to shape recovery [32,33]. Although this condition is detrimental to SME, it is essential to reduce the Mn content in these alloys, as high Mn content is detrimental to corrosion resistance [22]. In contrast, the absence of martensite-α′ in the microstructure of the SMSS B can be attributed to the high Co content, which reduces the stacking fault energy and favors the γ → ε transformation [34]. In addition, Co stabilizes the austenite phase by lowering the Néel transition temperature (T_N) [35], which increases the amount of austenite available for strain-induced transformation.

Fig. 2 shows the variation of OCP with time for Fe–Mn–Si–Cr–Ni-(Co) SMSSs and SS 304 L in 6 M and 11.5 M HNO_3 solutions. The OCP values for both alloy types gradually shift to more noble potentials, and their stabilization values increase with higher HNO_3 concentration. This behavior can be attributed to the continuous formation of the oxide film on the surface of the different samples. Similar behavior was reported by Ningshen et al. [6,36] for stainless steels exposed to concentrated nitric acid solutions. In addition, SS 304L exhibited the most noble OCP values in both acid concentrations, reaching approximately 702 ± 28 mV_{SCE} in 6 M and 712 ± 12 mV_{SCE} in 11.5 M HNO_3. Comparing SMSS A and SMSS B, the former showed higher OCP values with 595 ± 12 mV_{SCE} in 6 M and 697 ± 16 mV_{SCE} in 11.5 M HNO_3, while SMSS B showed the lowest values with 554 ± 23 mV_{SCE} in 6 M and 670 ± 5 mV_{SCE} in 11.5 M HNO_3. It is generally assumed that the nobler the OCP value of a given material in the passive range, the higher its passivation ability [9,17,37]. However, in highly oxidizing solutions, a higher OCP value can also mean heavy polarization and an increased corrosion rate [36,38]. In addition, for stainless alloys, it should be noted that due to the highly oxidizing nature of concentrated HNO_3 solutions, excessive ennoblement of the OCP is undesirable as it may lead to the attainment of the transpassive potential region. This transition would result in significantly higher corrosion rates due to transpassive corrosion and preferential attack along grain boundaries [4,16].

Fig. 3 shows representative Nyquist and Bode plots of Fe–Mn–Si–Cr–Ni-(Co) SMSSs and SS 304L samples in 6 M and 11.5 M HNO_3 solutions. The diameter of the capacitive semicircle differs among the alloys in the Nyquist plots, which is directly related to the charge transfer resistance at the metal–electrolyte interface and the level of protection provided by the passive films. In the 6 M HNO_3 solution [Fig. 3 (a)], SS 304L has the largest semicircle diameter, followed by SMSS B, then SMSS A. A similar trend is observed in the 11.5 M HNO_3 solution [Fig. 3 (c)], though SS 304L and SMSS B have slightly smaller semicircle diameters. In contrast, SMSS A shows a significant decrease in semicircle diameter, indicating a substantial reduction in passive film resistance [9,38]. In the Bode plots, which present the impedance modulus (|Z|) and phase angle (θ) as functions of frequency (f) [Fig. 3 (b–d)], two distinct frequency regions can be identified. In the high frequency region (i), |Z| remains relatively constant and the phase angle

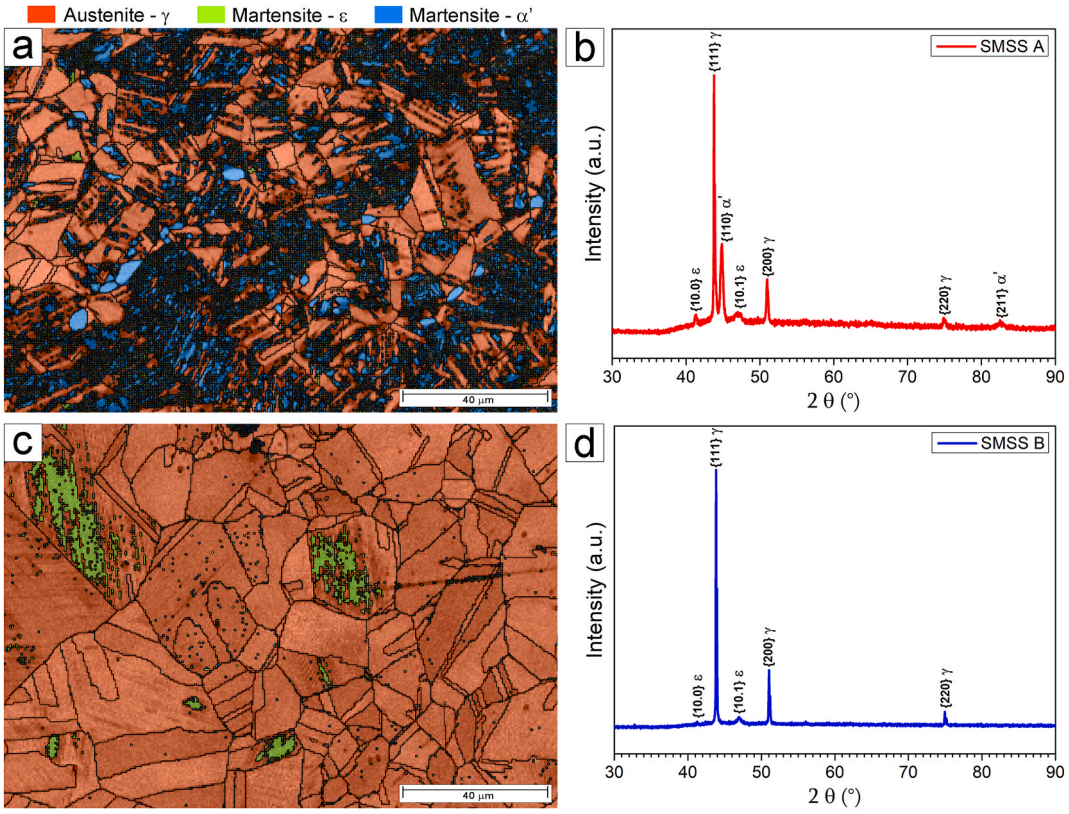

Fig. 1. EBSD phase maps and XRD patterns of the microstructure of SMSS A (a, b) and SMSS B (c,d).

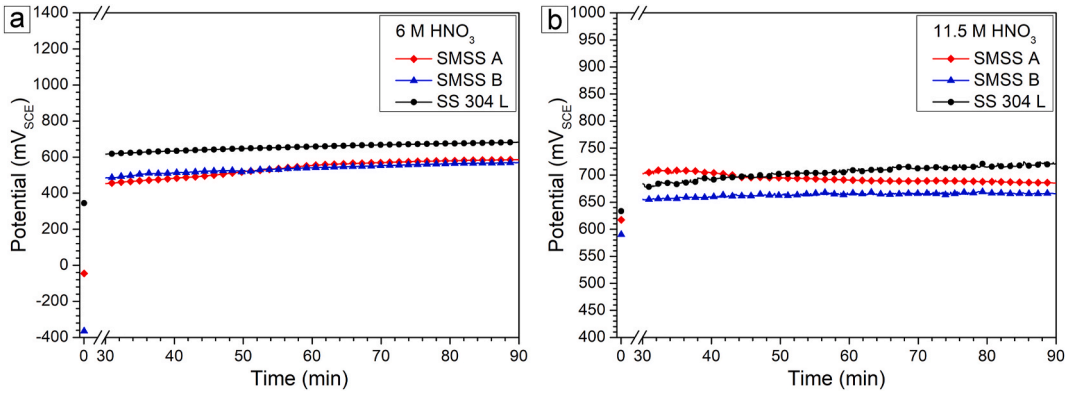

Fig. 2. Variation of OCP with time for Fe–Mn–Si–Cr–Ni-(Co) SMSSs and SS 304 L in HNO_3 solutions: (a) 6 M and (b) 11.5 M.

approaches 0°, indicating a predominantly resistive response controlled by the solution resistance. In contrast, the mid-to-low frequency region (ii) is characterized by a slope of |Z| vs. f close to −1, with the phase angle reaching its maximum values - features commonly associated with capacitive behavior. In addition, the Bode plots show a double phase angle peak, indicating the presence of two distinct relaxation time constants: one in the mid-frequency range and another at lower frequencies. This response is consistent with the formation of a passive film with a bilayer structure [39], where the inner, compact barrier layer is responsible for the low-frequency time constant, while the outer, porous layer corresponds to that observed at intermediate frequencies. It is also worth noting that the |Z| at a fixed frequency of 0.01 Hz, often used as an estimate of the polarization resistance of the material [21], reaches values of the order of 10^5 Ω cm^2 for SS 304L at both HNO_3 solutions. In comparison, the SMSSs exhibit lower |Z| values, on the order of 10^4 Ω cm^2, with SMSS B exhibiting significantly higher |Z| than SMSS A.

Electrochemical reactions at the metal-solution interface are commonly described by impedance models that simulate their behavior through an electronic circuit composed of resistors and capacitors. To provide a quantitative interpretation of the EIS measurements, the data were fitted with a complex Randles equivalent electric circuit (EEC), as shown in the Nyquist plots [Fig. 3(a–c)]. The best fits yielded X^2 values between 10^{-4} and 10^{-3}, consistent with a bilayer model of the passive film. This EEC is composed of a resistor (R_s), which represents the solution resistance, connected in series with a parallel combination (CPE_{po}//R_{po}), which characterizes the interface between the porous oxide film and the electrolyte at intermediate frequencies. In sequence, another parallel combination (CPE_b//R_b) accounts for the barrier properties of the passive film at low frequencies. Constant phase elements (CPEs) were used instead of ideal capacitors to more accurately describe the capacitance of the real oxide film, considering the presence of impurities, surface roughness and defects [40–42]. The impedance of

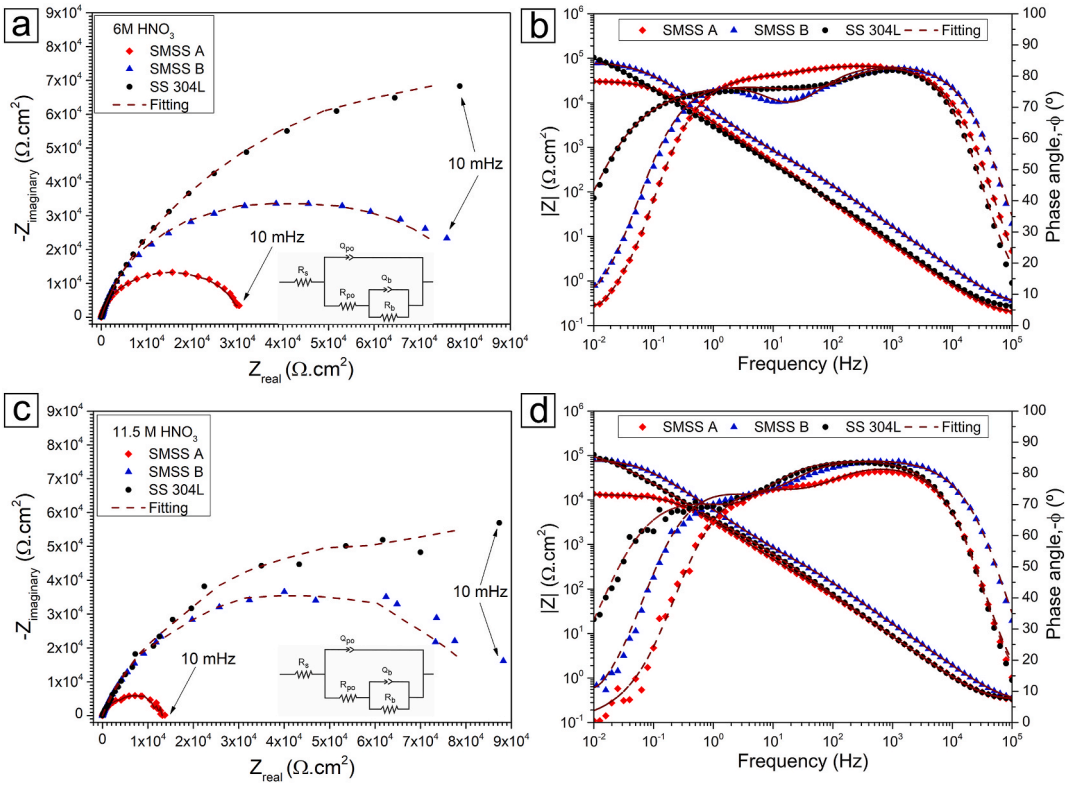

Fig. 3. Nyquist and Bode plots for Fe–Mn–Si–Cr–Ni-(Co) SMSSs and SS 304L in (a,b) 6 M and (c,d) 11.5 M HNO_3 solutions.

a CPE (Z_{CPE}) is defined by Equation (1):

$$Z_{CPE} = [Q(j\omega)^{\alpha}]^{-1} \quad (1)$$

The parameter Q represents the capacitance of the oxide layer, while j is the imaginary unit and ω is the angular frequency. The exponent α describes deviations from ideal capacitive behavior. When $\alpha = 1$, the CPE behaves as an ideal capacitor, while values in the range $0.5 < \alpha < 1$ indicate a distribution of dielectric relaxation times in the frequency domain. When $\alpha = 0.5$, the CPE models a Warburg impedance reflecting a diffusion dominated process [21].

The values of the EEC parameters obtained by fitting the experimental EIS data are presented in Table 2, and the fitted curves are shown as dashed lines in the Nyquist and Bode plots of Fig. 3. It can be observed that the estimated Rs values are quite low for all alloys, ranging from 0.18 to 0.35 Ω cm^2, and do not change significantly with increasing HNO_3 concentration. A comparative analysis between R_b and R_{po} at both HNO_3 concentrations shows that the inner barrier layer provides superior corrosion resistance, as evidenced by consistently higher R_b values relative to R_{po}. In addition, the average α_{po} and α_b values associated with the CPE exceed 0.80, a characteristic indicative of predominantly capacitive behavior. This suggests the formation of a highly corrosion resistant passive film on the alloy surfaces. With respect to R_b, SS 304L exhibits the highest corrosion resistance at both HNO_3 concentrations, with values of 1.64×10^5 Ω cm^2 in 6 M and 1.28×10^5 Ω cm^2 in 11.5 M HNO_3. The similarity of these values, considering the standard deviation, suggests that the passive film remains highly protective despite the increase in acid concentration. For SMSS B, R_b is 8.23×10^4 Ω cm^2 in 6 M, with minimal variation in 11.5 M HNO_3 (9.06×10^4 Ω cm^2). Although these values are lower than those of SS 304L, the passive film remains stable, ensuring effective corrosion protection even in the more aggressive environment. In contrast, SMSS A exhibits significantly lower R_b values, with 2.95×10^4 Ω cm^2 in 6 M, which decreases further to 1.72×10^4 Ω cm^2 in 11.5 M HNO_3. The decrease in R_b for SMSS A in 11.5 M HNO_3 suggests a destabilization of the passive film, likely due to enhanced ion transport and charge transfer processes at the film/electrolyte interface [43]. These conditions promote a higher reaction rate, contributing to the uniform dissolution of the passive film.

Fig. 4 shows the potentiodynamic polarization curves of Fe–Mn–Si–Cr–Ni-(Co) SMSSs and SS 304L in 6 M and 11.5 M HNO_3 solutions. The SMSSs in both media exhibit anodic behavior comparable to that of SS 304L, with spontaneous passivation without active-passive transition, low passive current densities (i_{pass}) in the μA/cm^2 range over the entire passive region, and transpassive breakdown potentials (E_{TP}) above 1000 mV_{SCE}. The increase in the current density value in the transpassive region is due to the oxidation of Cr(III) species present in the passive film (Cr_2O_3) to soluble Cr(VI) species (CrO_3) [44,45]. It is important to mention that a well-defined passive plateau is less evident

Table 2
Summary of EIS fitting parameters derived from EEC modeling describing the electrochemical behavior of Fe–Mn–Si–Cr–Ni-(Co) SMSSs and SS 304L in 6 M and 11.5 M HNO_3 solutions.

Alloy	Solution	R_s (Ω.cm^2)	R_{po} (Ω.cm^2)	Q_{po}(μS.s^a)/cm^2)	α_{po}	R_b(Ω.cm^2)	Q_b (μS.s^a)/cm^2)	α_b	X^2 (10^{-4})
SMSS A	6 M HNO_3	0.18 ± 0.01	2250 ± 1050	40.87 ± 0.13	0.94 ± 0.01	29450 ± 1050	11.47 ± 2.02	0.83 ± 0.01	1.54 ± 0.29
SMSS B		0.28 ± 0.01	1190 ± 100	24.60 ± 0.95	0.95 ± 0.01	82300 ± 1230	16.24 ± 8.90	0.83 ± 0.05	5.33 ± 2.06
SS 304L		0.26 ± 0.01	250 ± 20	35.01 ± 5.43	0.94 ± 0.01	164050 ± 36130	34.56 ± 8.68	0.81 ± 0.02	7.35 ± 1.69
SMSS A	11.5 M HNO_3	0.31 ± 0.01	1150 ± 960	30.94 ± 2.52	0.94 ± 0.01	17170 ± 5950	28.14 ± 2.56	0.82 ± 0.04	14.27 ± 0.76
SMSS B		0.34 ± 0.02	3770 ± 590	21.78 ± 0.37	0.94 ± 0.01	90590 ± 8940	16.96 ± 0.64	0.81 ± 0.04	10.30 ± 5.74
SS 304L		0.30 ± 0.03	3740 ± 640	30.54 ± 0.39	0.94 ± 0.01	128000 ± 8770	33.25 ± 0.23	0.81 ± 0.03	11.61 ± 2.04

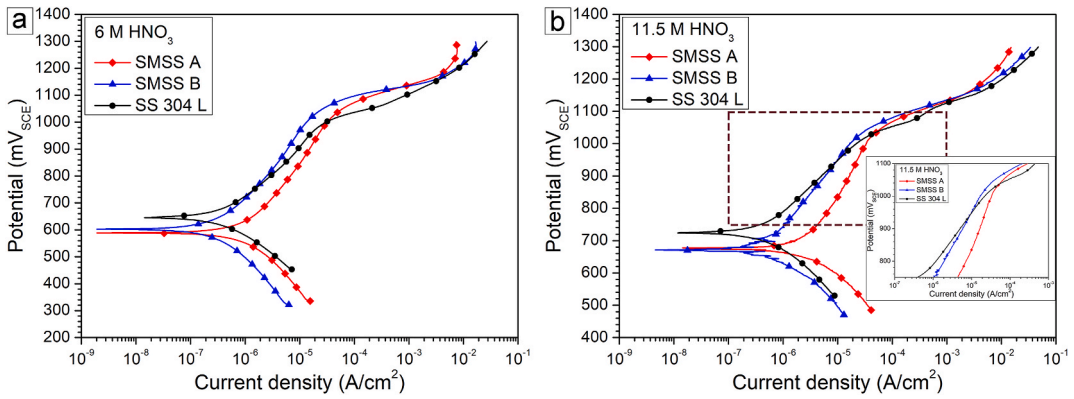

Fig. 4. Potentiodynamic polarization curves of Fe–Mn–Si–Cr–Ni-(Co) SMSSs and SS 304L in HNO_3 solutions: (a) 6 M and (b) 11.5 M. Adapted and modified from Ref. [29].

in potentiodynamic curves in highly oxidizing nitric acid. This is due to the aggressive nature of the medium and the tendency toward early transpassive processes. However, the low and relatively stable anodic current densities observed over a wide potential interval support the interpretation of passive-like behavior. This interpretation is consistent with previous studies that have reported similar electrochemical responses for stainless steels under strongly oxidizing conditions [6,38].

The electrochemical corrosion parameters, including corrosion potential (E_{corr}), passive current density (i_{pass}), and transpassive breakdown potential (E_{TP}), were determined from the polarization curves and are presented in Table 3. The i_{pass} values were determined at +800 mV_{SCE}, which is approximately half of the passive region for all alloys exposed to 6 M HNO_3 [Fig. 4 (a)]. Although 11.5 M HNO_3 shifts the passive region towards higher electrode potentials, i_{pass} was still determined at +800 mV_{SCE} to allow a direct comparison of the effect of increasing HNO_3 concentration. As previously noted in the OCP behavior of the two types of alloys, E_{corr} increases with increasing nitric acid concentration, with SMSSs showing lower values in both HNO_3 solutions compared to SS 304L.

This shift toward more noble potentials can be attributed primarily to an increase in the oxidizing power of the electrolyte due to the higher redox potential of concentrated nitric acid [46,47]. In such media, the dominant cathodic reaction involves the reduction of nitrate ions (NO_3^-), which proceeds via intermediate formation of nitrous acid (HNO_2) and promotes the generation of nitrogen oxides such as NO and NO_2 [6,38]. These species act as secondary oxidants that enhance cathodic kinetics, thereby shifting the mixed potential toward nobler values [36,48]. Concurrently, the elevated oxidizing capacity of the solution increases the susceptibility of the Cr_2O_3-enriched passive film to oxidation and dissolution, which can narrow the passive range and favor transpassive behavior [36]. Thus, the increase in E_{corr} with increasing HNO_3 concentration reflects both the acceleration of cathodic reactions and the destabilization of the passive film due to aggressive oxidants formed in solution.

The i_{pass} values for each alloy remain essentially unchanged with increasing HNO_3 concentration, taking into account the standard deviation. Among the alloys tested, SS 304L has the lowest i_{pass} values in both solutions, which is consistent with the EIS results, indicating that the passive film formed on SS 304L provides a more protective barrier against corrosion. However, at higher electrode potentials, the i_{pass} for SMSS B becomes slightly lower than that of SS 304L, as shown in Fig. 4, suggesting that its passive film provides superior protection under these conditions. When comparing the two SMSS, although both alloys exhibit values within the same order of magnitude, SMSS B consistently exhibits a lower i_{pass}. These differences are directly related to the Cr content, with SMSS A having the highest i_{pass} values due to its lower Cr content [49]. From Tables 3 and it can also be seen that the E_{TP} values for SMSSs are marginally higher than those of SS 304 L in both HNO_3 solutions, indicating that the passive films formed have greater stability in oxidizing environments. In addition, it is worth noting that despite the low Cr content of SMSSs (9.92–12.80 wt%) the efficiency of the passive film protection is comparable to that of SS 304 L (19.28 wt%). This can be directly related to the incorporation of Si into the passive film of SMSSs [4,21,22,50,51].

Table 3
Comparative electrochemical parameters for SMSSs and SS 304L obtained from potentiodynamic polarization curves in 6 M and 11.5 M HNO_3 (i_{pass} values were taken at +800 mV_{SCE}).

Alloy	Solution	E_{corr} (mV_{SCE})	i_{pass} ($\mu A/cm^2$)	E_{TP} (mV_{SCE})
SMSS A	6 M HNO_3	579 ± 14	8.06 ± 1.44	1072 ± 2
SMSS B		586 ± 23	3.81 ± 1.65	1079 ± 23
SS 304 L		682 ± 30	0.94 ± 0.38	1041 ± 4
SMSS A	11.5 M HNO_3	682 ± 6	8.83 ± 1.52	1059 ± 12
SMSS B		663 ± 11	2.29 ± 0.44	1078 ± 4
SS 304 L		721 ± 16	0.69 ± 0.30	1053 ± 5

Fig. 5 shows OM images of the surface morphology of Fe–Mn–Si–Cr–Ni-(Co) SMSSs and SS 304L after potentiodynamic polarization in 6 M HNO_3 and SEM images corresponding to tests performed in 11.5 M HNO_3. Although SMSS A contains a significant amount of α′-martensite partially distributed along grain boundaries (Fig. 1) and this phase has been reported to dissolve selectively in acidic solutions [52,53], no signs of intensified corrosion or IGC were detected. Instead, SMSS A exhibited subtle corrosion similar to SMSS B under both HNO_3 concentrations, as shown in Fig. 5(a–d), with no perceptible difference in corrosion extent or morphology between samples. Additionally, small pits are visible on the SMSS surfaces at both HNO_3 concentrations. These pits are likely due to localized corrosion initiated at the interfaces of Mn oxysulfide inclusions [22,24], which are known to form in these alloys due to their higher Mn content compared to conventional stainless steels. These inclusions are well documented to be susceptible to selective dissolution [54].

In contrast, SS 304L [Fig. 5(e and f)] suffered the most severe attack, which was predominantly located at the grain boundaries at both HNO_3 concentrations. This IGC process is unlikely to be related to sensitization since SS 304L is in the solution-treated condition. Instead, it can be attributed to the segregation of Si and other impurity elements at grain boundaries, which can promote localized electrochemical activity. On the other hand, the absence of IGC in SMSSs can be attributed to their higher Si content (~5 wt%), homogeneously distributed throughout the matrix, ensuring a similar electrochemical response between grain boundaries and grain interiors. Previous studies [15,16,18] have shown that both the concentration and distribution of Si within the metallic matrix play a critical role in determining the susceptibility of stainless steels to IGC in highly oxidizing media.

Fig. 6 shows the Fe $2p_{3/2}$, Cr $2p_{3/2}$, Si 2p and O 1s high-resolution

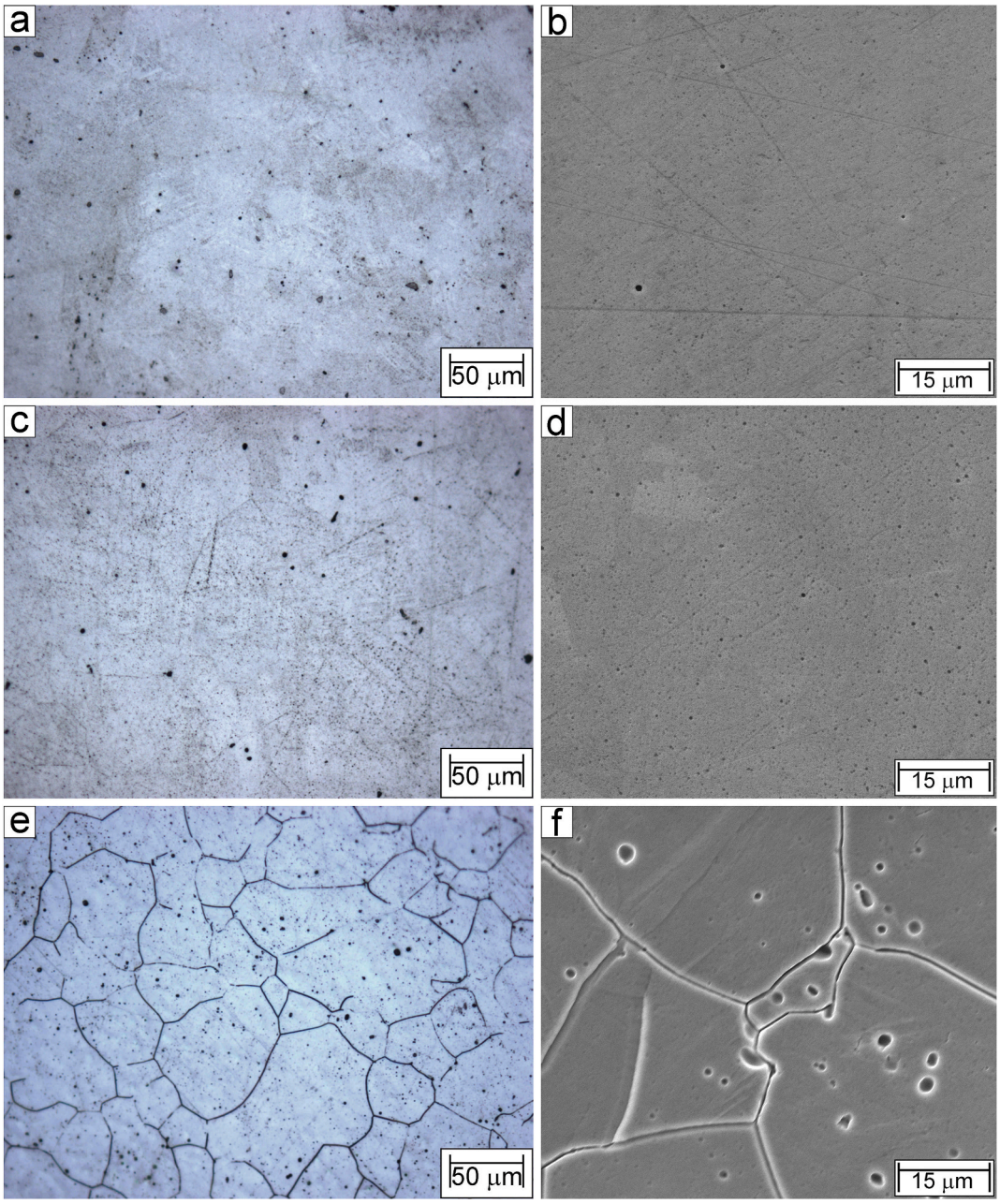

Fig. 5. Surface morphology of SMSSs and SS 304L after potentiodynamic polarization tests in HNO_3 solutions. OM images correspond to samples tested in 6 M HNO_3, while secondary electron (SE)/SEM images correspond to samples tested in 11.5 M HNO_3: (a, b) SMSS A, (c, d) SMSS B, and (e, f) SS 304L.

XPS spectra of the passive films formed for 1 h on Fe–Mn–Si–Cr–Ni-(Co) SMSSs and SS 304L at +800 mV_{SCE} in 11.5 M HNO_3 solution. The high-resolution Fe $2p_{3/2}$ spectra presented in Fig. 6 (a) reveal the presence of metallic Fe (706.7 eV) and Fe oxides and hydroxides, including sub-stoichiometric FeO_x (707.7 eV), FeO (709.4 eV), Fe_2O_3 (710.9 eV), and FeOOH (712.4 eV). Considering an XPS sampling depth of <5 nm, the disappearance of the metallic phase of the underlying steel suggests a thicker passive layer of SMSS A compared to that of SMSS B and SS 304L. The high-resolution Cr $2p_{3/2}$ spectra shown in Fig. 6 (b) are mainly characterized by two peaks: the one with the lowest binding energy (574.0 eV) corresponds to metallic Cr, while the peak at about 577 eV is commonly attributed to Cr(III) oxides (576.0 eV) and hydroxides (577.3 eV) [55–57]. However, to obtain an optimal fit to the experimental spectra, an additional component at about 578.5 eV was required, which is associated with the CrO_3 phase in the passive film [58]. The detection of small amounts of Cr(VI) oxide (578.5 eV) in the passive film of the alloys appears to be related to the highly oxidizing nature of the 11.5 M HNO_3 solution.

For Si [Fig. 6 (c)], analysis of the high-resolution spectra for the SMSS B sample revealed three distinct peaks at 99.6 eV, 102.2 eV, and 103.3 eV, corresponding to metallic Si and its oxidized forms SiO_x and SiO_2, respectively. For the SMSS A sample, only the SiO_2 phase was detected due to the thicker passive film. It is important to note that the exact chemical state of Si in passive films remains a topic of discussion. Some studies [59,60] suggest that Si(IV) (103.5 eV) is predominantly found as a continuous SiO_2 layer within the passive film. In contrast, Loka et al. [61] identified two oxidation states of Si in the passive film, indicating the coexistence of SiO_2 [Si(IV)] and SiO [Si(II)], the latter exhibiting a binding energy of 102.3 eV. In addition, Rovere et al. [21, 22] and Robin et al. [18] observed Si in the passive film of stainless steels with a binding energy of 101.9 eV, which they attributed to the presence of an Fe–Cr mixed silicate [$(SiO_4)^{4-}$] rather than SiO_2. In this study, Si

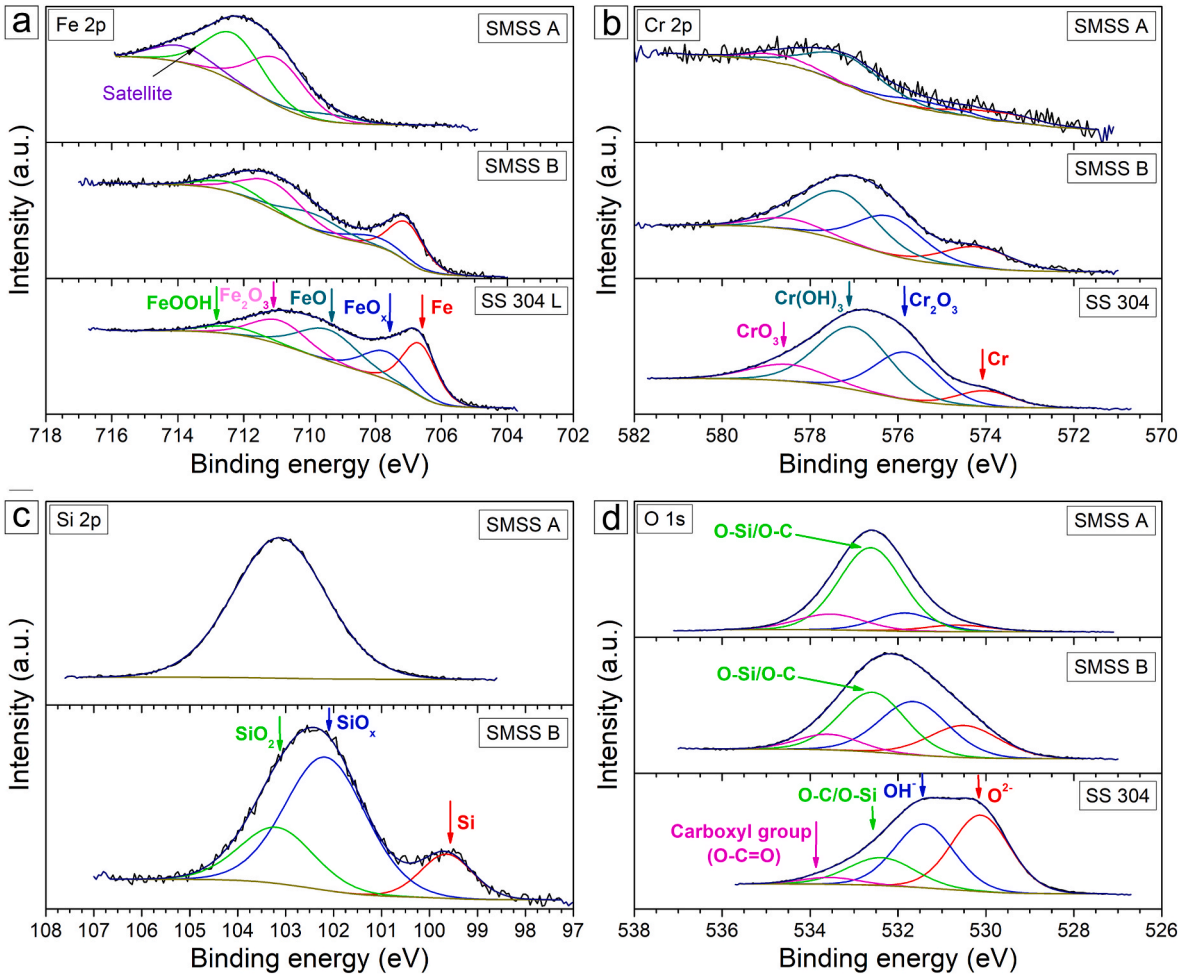

Fig. 6. High-resolution XPS spectra of the passive films formed on Fe–Mn–Si–Cr–Ni-(Co) SMSSs and SS 304L after 1 h of exposure at +800 mV_{SCE} in 11.5 M HNO_3 solution: (a) Fe $2p_{3/2}$, (b) Cr $2p_{3/2}$, (c) Si 2p, and (d) O 1s ionizations. Adapted and modified from Ref. [29].

detected in the passive layer of Fe–Mn–Si–Cr–Ni-(Co) SMSSs after exposure to 11.5 M HNO_3 showed a binding energy of about 103.3 eV, which is in close agreement with the reported values for SiO_2. Finally, the O 1s spectra show the presence of metal lattice oxygen at about 530 eV, surface hydroxyl groups at 531.5 eV followed by O–Si bonds at 532.7 eV, the latter constituting the most prominent intensity for the SMSS samples [Fig. 6 (d)]. Some contributions of oxidized adventitious carbon (O–C and O–C═O) bond are also present.

The identified metallic elements were attributed to the underlying substrate, while the composition of the passive film was determined based on the peak fraction of Fe, Cr, and Si cations. Fig. 7 shows the atomic percentage (at.%) of cations in the passive films formed on Fe–Mn–Si–Cr–Ni-(Co) SMSSs and SS 304L. The passive film on SS 304L is predominantly composed of Cr, accounting for approximately 56 at.% of the cationic species, which is consistent with the values reported by Olsson and Landolt [39], who indicated that Cr(III) typically represents 50 to 70 at.% of the passive film cations in stainless steels exposed to acidic environments. In contrast, the passive films on the Fe–Mn–Si–Cr–Ni-(Co) SMSSs are mainly composed of Si, with a concentration of 72.5–84.9 at.%, which represents an almost eightfold increase compared to its content in the matrix (~10 at.%). This enrichment suggests that Si is preferentially incorporated into the passive layer during film growth. On the other hand, the comparatively lower concentrations of Cr and Fe indicate a selective dissolution of these elements during passive film development.

It is well known that the high corrosion resistance of stainless steels with Cr contents above 12 wt% in oxidizing acid solutions is due to the formation of a protective passive film consisting mainly of hydrated Cr (III) oxyhydroxides [6,49], which is in agreement with the XPS results obtained for SS 304L. In the case of the SMSSs, the Cr content in the passive film formed on SMSS B is low and practically negligible for SMSS A. For these alloys, the high protectiveness of the passive films formed on Fe–Mn–Si–Cr–Ni-(Co) SMSSs in HNO_3 solutions is apparently

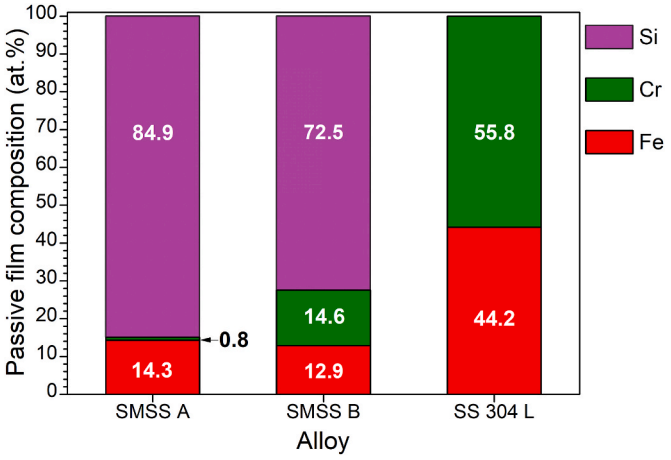

Fig. 7. Cationic composition (at.%) of passive films formed after 1 h at +800 mV_{SCE} in 11.5 M HNO_3 on Fe–Mn–Si–Cr–Ni-(Co) SMSSs and SS 304L.

associated with a Si-rich passive film containing approximately 72–85 at.% Si ions relative to the total content of Fe, Cr, and Si ions. However, a Si-rich passive film with low Cr content is considered less effective than a Cr_2O_3 film in providing corrosion resistance in the passive region in concentrated nitric acid [18]. As a result, decreasing Cr content tends to reduce the effectiveness of the passive film, resulting in higher i_{pass} values (Table 2). On the other hand, at higher electrode potentials, the Si-rich film becomes more effective, leading to higher E_{TP} values and inhibiting generalized corrosion by suppressing cathodic reaction. This may be due to a decrease in the electronic conductivity of the passive film or an increase in the overpotential required for the cathodic process [18].

Despite their general use in nitric acid systems, several stainless steels have exhibited failure when exposed to HNO_3 solutions exceeding 8 M and temperatures above 80 °C [9]. Under such highly oxidizing and high-temperature conditions, corrosion resistance can vary significantly depending on the alloy composition. The oxidizing power of the solution is further enhanced by the generation of electroactive species such as HNO_2 and NO_2 via the cathodic reduction of NO_3^-. This process is intensified in the presence of dissolved metal ions such as Fe(III), Cr(VI), and others, which increase the redox potential and depolarize local electrochemical cells [38], potentially leading to the transpassive dissolution of the protective Cr(III) oxide layer into soluble Cr(VI) species [8,62]. The effect of these factors on corrosion resistance is illustrated in Fig. 8, which shows the corrosion rates of the SMSSs after 240 h of immersion in boiling 11.5 M HNO_3. SMSS A exhibited a corrosion rate of approximately 1.5 mm/y, while SMSS B exhibited a significantly lower rate of approximately 0.9 mm/y. For comparison, the reported corrosion rate for SS 304L under the same conditions is approximately 4.5 mm/y [63]. Thus, although SMSS A has a higher corrosion rate than SMSS B, the corrosion resistance of both is significantly superior to that of SS 304L. This improved performance is due to the formation of a protective Si-rich passive film of silicon oxides that improves corrosion resistance to the highly oxidizing nature of boiling nitric acid.

The superior corrosion resistance of SMSS B compared to SMSS A is primarily due to its higher Cr content (12.80 wt% versus 9.92 wt%), which approaches the lower limit typically required for passivation in boiling nitric acid. In such highly oxidizing environments, the corrosion rate of pure Fe can exceed 10,000 mm/y, but decreases progressively with Cr additions. Alloys containing about 4.5 wt% Cr exhibit rates close to 4000 mm/y, decreasing to about 40 mm/y at 8 wt%, 3 mm/y at 17 wt %, and as low as 0.2 mm/y at 25 wt% Cr [4]. While Cr is essential for the formation of a protective Cr_2O_3-based passive film, the beneficial effect

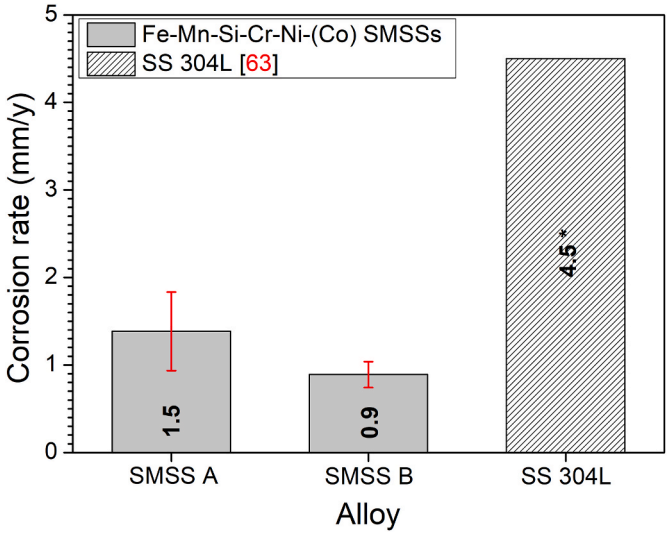

Fig. 8. Corrosion rates of the Fe–Mn–Si–Cr–Ni-(Co) SMSSs after 240 h of immersion in boiling 11.5 M HNO_3.

of Si should not be overlooked. The presence of a high Si content complements the effect of Cr and contributes to the formation of a more stable and protective passive film on both SMSSs. According to Raj and Mudali [4], stainless steels are considered suitable for nitric acid service if corrosion rates remain below 0.45 mm/y, with an upper limit of 0.6 mm/y for non-critical applications. Although the SMSSs evaluated do not yet meet these regulatory criteria, the significantly better performance of SMSS B compared to 304L SS suggests that by slightly increasing Cr content and maintaining high Si content, it may be possible to develop stainless steels that meet both performance and regulatory criteria without relying on costly corrosion resistant alloys.

The protective effect of a Si-rich passive film is limited under highly oxidizing conditions, particularly when not supported by sufficient Cr content. In SMSS A, the passive film formed was composed predominantly of the SiO_2 phase, as shown in Fig. 6 (c) and 7, but this oxide layer did not provide superior corrosion resistance in boiling nitric acid compared to SMSS B. This finding suggests that a minimum Cr content in the passive film is essential to ensure effective protection. According to Laurent et al. [64], although Si alloying does not affect the Cr dissolution in its hexavalent state, it can prevent Cr dissolution under transpassive conditions, which contributes to improved corrosion resistance when both elements are present. Thus, a balanced incorporation of Cr and Si in the passive film appears to be necessary to achieve optimal performance in boiling nitric acid. The limited protective effect of a pure SiO_2 film compared to a mixed Cr–Si oxide can be understood from the morphology of the corrosion product observed on SMSS A after boiling 11.5 M HNO_3, shown in Fig. 9 (a). The corrosion product exhibits extensive cracking and spallation, exposing the metallic substrate to the electrolyte and accelerating the corrosion process. The EDS line scan profile analysis shown in Fig. 9 (b) indicates that the corrosion product is composed mainly of Si with no detectable Cr. In addition, XRD analysis of the corrosion product on substrate shown in Fig. 9 (c) revealed a broad amorphous halo in the $15° < 2\theta < 30°$ region along with crystalline peaks corresponding to the underlying microstructure due to the high penetration depth of X-rays. Grazing incidence XRD analysis confirmed the amorphous nature of the SiO_2 layer, in agreement with a previous study [23]. These results suggest that the poor protectiveness of the SiO_2 film is not only due to its composition, but also to its weak adhesion due to high intrinsic stress, which promotes cracking and spallation, allowing electrolyte access to the metal surface and compromising overall corrosion resistance.

4. Conclusions

In this study, the electrochemical behavior and passive film characteristics of two Fe–Mn–Si–Cr–Ni-(Co) SMSSs were evaluated in comparison to conventional SS 304L when exposed to highly oxidizing nitric acid environments. The electrochemical results are highly consistent and in good agreement with the observed surface morphologies after corrosion, the chemical composition of the passive films, and the corrosion rates obtained in boiling 11.5 M HNO_3. The following conclusions are drawn:

1. The SMSSs exhibited distinct microstructural features influenced by their chemical composition. SMSS A has a multiphase microstructure composed of austenite, martensite-α′, and martensite-ε, while SMSS B is predominantly austenitic with a small amount of martensite-ε. These differences are related to the high Co content in SMSS B, which favors austenite stability;
2. EIS results indicate that the passive films formed on the alloys at room temperature consist of a bilayer structure consisting of an outer porous layer and an inner barrier layer, the latter playing a key role in corrosion protection. The passive films on SS 304L and SMSS B exhibited good stability in both 6 M and 11.5 M HNO_3 solutions, while the stability of the film on SMSS A decreased with increasing HNO_3 concentration. Furthermore, the corrosion resistance of the

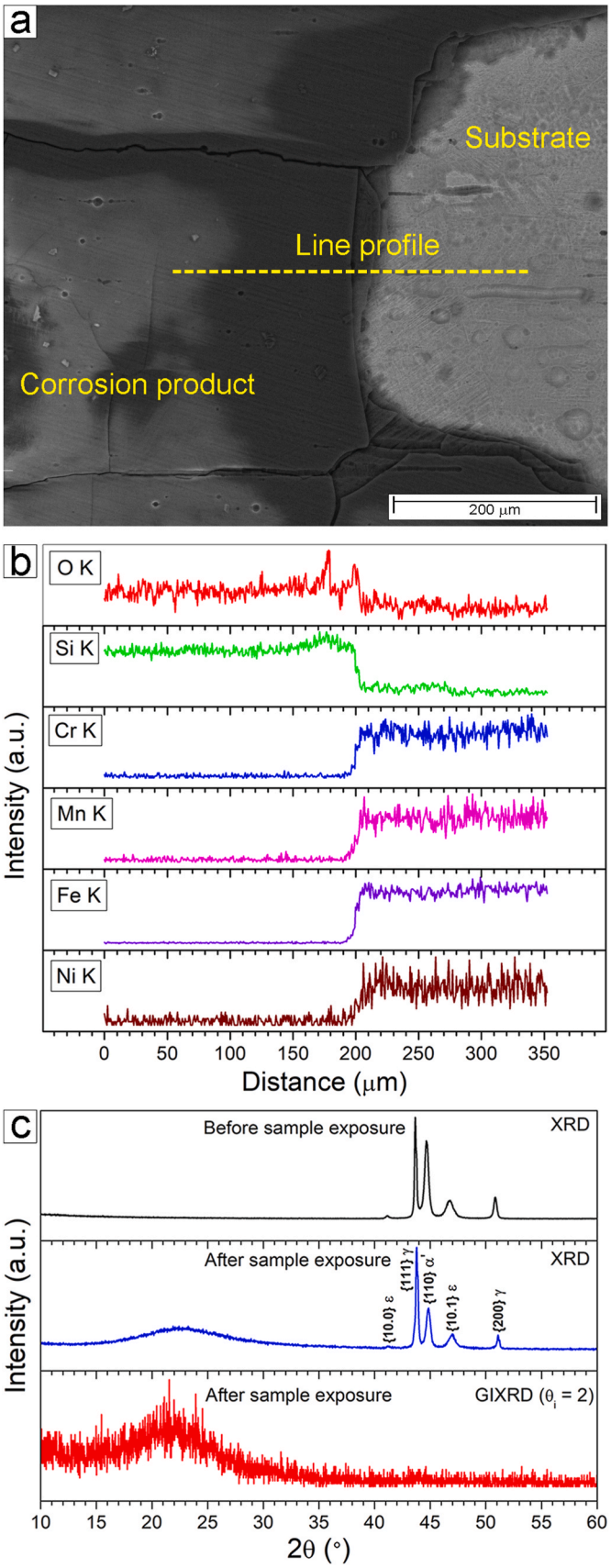

Fig. 9. (a) Surface morphology of SMSS A after immersion in boiling 11.5 M HNO_3, (b) EDS line scan profile along the yellow line, and (c) XRD pattern of the substrate before immersion, the corrosion product after immersion, and grazing incidence XRD (2° angle of incidence) of the corrosion product.

passive film followed the order: SS 304L > SMSS B > SMSS A, in both nitric acid solutions;

3. All alloys exhibited spontaneous passivation in both 6 M and 11.5 M HNO_3 solutions, with the SMSSs showing good passive behavior despite their low Cr content. SS 304L exhibited the lowest i_{pass} values at +800 mV_{SCE}; however, at higher potentials, its current densities became higher than those of SMSS B. The E_{TP} values of the SMSSs were slightly higher than those of SS 304L in both acid concentrations. While SMSSs exhibited generalized corrosion, SS 304L exhibited intergranular corrosion that became more pronounced with increasing nitric acid concentration;
4. The high protectiveness of passive films formed on Fe–Mn–Si–Cr–Ni–(Co) SMSSs in HNO_3 solutions is mainly attributed to their high Si content (about 72–85 at.%) in the form of silicon oxides highlighting the high potential of these alloys. This is particularly valid for SMSS B, as a promising material for applications in highly oxidizing environments such as spent nuclear fuel reprocessing. However, a passive film composed only of Si, without any Cr enrichment, is not sufficient to ensure stability under aggressive conditions. This limitation is related to the poor adhesion of the oxide layer to the substrate for SMSS A, which exhibits extensive cracks and spallation regions, thus accelerating the corrosion rate in boiling 11.5 M HNO_3. These results highlight the importance of a sensitive synergistic balance between Si and Cr contents in the passive film to achieve effective corrosion resistance in highly oxidizing environments.

Data availability

The data supporting the findings of this research are available in the paper. Any supplementary information or explanation is available from the corresponding author upon request.

Declaration of competing interest

The authors certify that they have no affiliations with or involvement in any organization or entity with any financial interest, or non-financial interest in the subject matter or materials discussed in this manuscript.

Acknowledgements

The authors thank PPGCEM/UFSCar (Postgraduate Program in Materials Science and Engineering of the Federal University of São Carlos) and the Brazilian research funding agency CNPq (National Council for Scientific and Technological Development – Grant Nos. 460659/2014-6, 312614/2020-9, and 315903/2023-6) for financial support. The authors also acknowledge the permission to use the facilities of the Laboratory of Structural Characterization (LCE/DEMa/UFSCar). This study was financed in part by the Coordenação de Aperfeiçoamento de Pessoal de Nível Superior - Brasil (CAPES) - Finance Code 001.

References

[1] Xie Y, Wang J, Sun Q, Hu Y, Men M, Wang S, Liu G, Mi A. Effect of strontium and cesium on corrosion and contamination of 316L stainless steels during spent nuclear fuel reprocessing. Prog Nucl Energy 2022;154:104453. https://doi.org/10.1016/j.pnucene.2022.104453.

[2] Liu Z, Zhang LM, Chen WQ, Ma AL, Zheng Y, Yan W, Li YF, Daniel EF, Shan YY, Zheng YG. Effect of oxidizing ions on the corrosion behavior of SiN stainless steel in high-temperature nitric acid solution. Electrochim Acta 2023;442:141917. https://doi.org/10.1016/j.electacta.2023.141917.

[3] Nash KL, Nilsson M. Introduction to the reprocessing and recycling of spent nuclear fuels. In: Reprocess. Recycl. Spent nucl. Fuel. Elsevier; 2015. p. 3–25. https://doi.org/10.1016/B978-1-78242-212-9.00001-0.

[4] Raj B, Mudali UK. Materials development and corrosion problems in nuclear fuel reprocessing plants. Prog Nucl Energy 2006;48:283–313. https://doi.org/10.1016/j.pnucene.2005.07.001.

[5] Irisawa E, Kato C. Estimating the corrosion rate of stainless steel R-SUS304ULC in nitric acid media under concentrating operation. J Nucl Mater 2024;591:154914. https://doi.org/10.1016/j.jnucmat.2024.154914.

[6] Ningshen S, Sakairi M. Corrosion degradation of AISI type 304L stainless steel for application in nuclear reprocessing plant. J Solid State Electrochem 2015;19:3533–42. https://doi.org/10.1007/s10008-015-2891-y.
[7] He P, Wang X, Zheng K, Jiang Y, Li J, Sun Y. A different type of intergranular corrosion facilitated by hydrogen in austenitic stainless steel. Corros Sci 2023;219:111258. https://doi.org/10.1016/j.corsci.2023.111258.
[8] Fauvet P, Balbaud F, Robin R, Tran Q-T, Mugnier A, Espinoux D. Corrosion mechanisms of austenitic stainless steels in nitric media used in reprocessing plants. J Nucl Mater 2008;375:52–64. https://doi.org/10.1016/j.jnucmat.2007.10.017.
[9] Ningshen S, Kamachi Mudali U, Amarendra G, Raj B. Corrosion assessment of nitric acid grade austenitic stainless steels. Corros Sci 2009;51:322–9. https://doi.org/10.1016/j.corsci.2008.09.038.
[10] Bague V, Chachoua S, Tran QT, Fauvet P. Determination of the long-term intergranular corrosion rate of stainless steel in concentrated nitric acid. J Nucl Mater 2009;392:396–404. https://doi.org/10.1016/j.jnucmat.2008.12.100.
[11] Raj B, Mudali UK, Jayakumar T, Kasiviswanathan KV, Natarajan R. Meeting the challenges related to material issues in chemical industries. Sadhana 2000;25:519–59. https://doi.org/10.1007/BF02703505.
[12] Tcharkhtchi-Gillard E, Benoit M, Clavier P, Gwinner B, Miserque F, Vivier V. Kinetics of the oxidation of stainless steel in hot and concentrated nitric acid in the passive and transpassive domains. Corros Sci 2016;107:182–92. https://doi.org/10.1016/j.corsci.2016.02.031.
[13] Gwinner B, Auroy M, Balbaud-Célérier F, Fauvet P, Larabi-Gruet N, Laghoutaris P, Robin R. Towards a reliable determination of the intergranular corrosion rate of austenitic stainless steel in oxidizing media. Corros Sci 2016;107:60–75. https://doi.org/10.1016/j.corsci.2016.02.020.
[14] Wang J, Liu Z, Tian H, Han P, Gonzalez-Garcia Y. Inhibition of the second phase precipitation and improvement of intergranular corrosion resistance by boron segregation at the grain boundary of S31254 superaustenitic stainless steel. Corros Commun 2024;15:1–12. https://doi.org/10.1016/j.corcom.2023.08.006.
[15] Kasparova OV. Peculiarities of intergranular corrosion of silicon-containing austenitic stainless steels. Prot Met 2004;40:425–31. https://doi.org/10.1023/B:PROM.0000043059.46578.f9.
[16] Mayuzumi M, Ohta J, Kako K, Kawakami E. Effect of silicon and manganese additions on the transpassive corrosion of high-purity Fe-18% Cr-14% Ni alloys. Corrosion 2000;56:910–20. https://doi.org/10.5006/1.3280594.
[17] Sedriks AJ. Corrosion of stainless steels. 2. ed. New York: John Wiley & Sons; 1996.
[18] Robin R, Miserque F, Spagnol V. Correlation between composition of passive layer and corrosion behavior of high Si-containing austenitic stainless steels in nitric acid. J Nucl Mater 2008;375:65–71. https://doi.org/10.1016/j.jnucmat.2007.10.016.
[19] Armijo JS, Wilde BE. Influence of Si content on the corrosion resistance of austenitic Fe-Cr-Ni alloys in oxidizing acids. Corros Sci 1968;8:649–64. https://doi.org/10.1016/S0010-938X(68)80100-3.
[20] Della Rovere CA, Alano JH, Otubo J, Kuri SE. Corrosion behavior of shape memory stainless steel in acid media. J Alloys Compd 2011;509:5376–80. https://doi.org/10.1016/j.jallcom.2011.02.051.
[21] Della Rovere CA, Alano JH, Silva R, Nascente PAP, Otubo J, Kuri SE. Characterization of passive films on shape memory stainless steels. Corros Sci 2012;57:154–61. https://doi.org/10.1016/j.corsci.2011.12.022.
[22] Della Rovere CA, Alano JH, Silva R, Nascente PAP, Otubo J, Kuri SE. Influence of alloying elements on the corrosion properties of shape memory stainless steels. Mater Chem Phys 2012;133:668–73. https://doi.org/10.1016/j.matchemphys.2012.01.049.
[23] Silva R, Arana C, de Sousa Malafaia AM, Mendes Filho AA, Pascal C, Otubo J, Sordi VL, Rovere CAD. Microstructure and surface oxidation behavior of an austenitic Fe-Mn-Si-Cr-Ni-Co shape memory stainless steel at 800 °C in air. Corros Sci 2019:108103. https://doi.org/10.1016/j.corsci.2019.108103.
[24] Silva R, Young DJ, Junior CBM, Vacchi GS, Alberto CAT, de S. Malafaia AM, Pascal C, Rovere CAD. Role of cerium addition in enhancing the oxidation resistance of austenitic Fe-Mn-Si-Cr-Ni shape memory stainless steels at 800 °C: microstructure and oxidation mechanism. Corros Sci 2022;209:110788. https://doi.org/10.1016/j.corsci.2022.110788.
[25] Kajiwara S. Characteristic features of shape memory effect and related transformation behavior in Fe-based alloys. Mater Sci Eng A 1999;273–275:67–88. https://doi.org/10.1016/S0921-5093(99)00290-7.
[26] da Silva R, Baroni LFS, Martins Junior CB, Camilo Magalhães DC, Vacchi GS, Kliauga AM, Lima NB, Otubo J, Della Rovere CA. Effect of cerium addition on the microstructure and shape memory properties of austenitic Fe–Mn–Si–Cr–Ni alloys. Adv Eng Mater 2024;26. https://doi.org/10.1002/adem.202301513.
[27] Silva R, Vacchi GS, Santos IGR, de Sousa Malafaia AM, Kugelmeier CL, Mendes Filho AA, Pascal C, Sordi VL, Rovere CAD. Insights into high-temperature oxidation of Fe-Mn-Si-Cr-Ni shape memory stainless steels and its relationship to alloy chemical composition. Corros Sci 2019:108269. https://doi.org/10.1016/j.corsci.2019.108269.
[28] Dai P, Zhou L. Investigation on the connecting strength of Fe-Mn-Si-C shape memory alloy pipe coupling. J Mater Sci 2006;41:3441–3. https://doi.org/10.1007/s10853-006-7933-5.
[29] della Rovere CA, Silva R, Hammer P, Otubo J, Kuri SE. Corrosion behavior of Fe-Mn-Si-Cr-Ni-Co shape memory stainless steel in highly oxidizing medium. Mater Sci Forum 2016;869:669–74. https://doi.org/10.4028/www.scientific.net/MSF.869.669.
[30] Surviliene S. The use of XPS for study of the surface layers of Cr–Co alloy electrodeposited from Cr(III) formate–urea baths. Solid State Ionics 2008;179:222–7. https://doi.org/10.1016/j.ssi.2007.12.052.
[31] NIST X-ray Photoelectron Spectroscopy Database. NIST standard reference database number 20. Gaithersburg MD, 20899: National Institute of Standards and Technology; 2000. https://doi.org/10.18434/T4T88k.
[32] Maji BC, Krishnan M, Gouthama, Ray RK. Role of Si in improving the shape recovery of FeMnSiCrNi shape memory alloys. Metall Mater Trans A 2011;42:2153–65. https://doi.org/10.1007/s11661-011-0651-x.
[33] Gu Q, Van Humbeeck J, Delaey L. A review on the martensitic transformation and shape memory effect in Fe-Mn-Si alloys. J Phys IV 1994;4:135–44. https://doi.org/10.1051/jp4:1994319.
[34] Jiang B, Xu K, Qi X, Zhou W. Effects of cobalt content on martensitic transformation and shape memory effect in Fe-Mn-Si-Cr-Ni alloys. J Phys IV 2003;112:393–6. https://doi.org/10.1051/jp4:2003909.
[35] Gartstein E, Rabinkin A. On the f.c.c. → h.c.p. phase transformation in high manganese-iron alloys. Acta Metall 1979;27:1053–64. https://doi.org/10.1016/0001-6160(79)90193-7.
[36] Ningshen S, Sakairi M, Suzuki K, Ukai S. The corrosion resistance and passive film compositions of 12% Cr and 15% Cr oxide dispersion strengthened steels in nitric acid media. Corros Sci 2014;78:322–34. https://doi.org/10.1016/j.corsci.2013.10.015.
[37] Padhy N, Ningshen S, Panigrahi BK, Kamachi Mudali U. Corrosion behaviour of nitrogen ion implanted AISI type 304L stainless steel in nitric acid medium. Corros Sci 2010;52:104–12. https://doi.org/10.1016/j.corsci.2009.08.042.
[38] Ningshen S, Kamachi Mudali U, Ramya S, Raj B. Corrosion behaviour of AISI type 304L stainless steel in nitric acid media containing oxidizing species. Corros Sci 2011;53:64–70. https://doi.org/10.1016/j.corsci.2010.09.023.
[39] Olsson C-OA, Landolt D. Passive films on stainless Steels—Chemistry, structure and growth. Electrochim Acta 2003;48:1093–104. https://doi.org/10.1016/S0013-4686(02)00841-1.
[40] Jorcin J-B, Orazem ME, Pébère N, Tribollet B. CPE analysis by local electrochemical impedance spectroscopy. Electrochim Acta 2006;51:1473–9. https://doi.org/10.1016/j.electacta.2005.02.128.
[41] Hirschorn B, Orazem ME, Tribollet B, Vivier V, Frateur I, Musiani M. Constant-phase-element behavior caused by resistivity distributions in films. J Electrochem Soc 2010;157:C452. https://doi.org/10.1149/1.3499564.
[42] Orazem ME, Frateur I, Tribollet B, Vivier V, Marcelin S, Pébère N, Bunge AL, White EA, Riemer DP, Musiani M. Dielectric properties of materials showing constant-phase-element (CPE) impedance response. J Electrochem Soc 2013;160:C215–25. https://doi.org/10.1149/2.033306jes.
[43] Jayaraj J, Ravi Shankar A, Kamachi Mudali U. Electrochemical and passive characterization of a beta type Ti45Zr38Al17 cast rod in nitric acid medium. Electrochim Acta 2012;85:210–9. https://doi.org/10.1016/j.electacta.2012.08.047.
[44] Song G. Transpassivation of Fe–Cr–Ni stainless steels. Corros Sci 2005;47:1953–87. https://doi.org/10.1016/j.corsci.2004.09.007.
[45] Pourbaix M, Zhang H, Pourbaix A. Presentation of an Atlas of chemical and electrochemical equilibria in the presence of a gaseous phase. Mater Sci Forum 1997;251–254:143–8. https://doi.org/10.4028/www.scientific.net/msf.251-254.143.
[46] Macdonald DD. Passivity–the key to our metals-based civilization. Pure Appl Chem 1999;71:951–78. https://doi.org/10.1351/pac199971060951.
[47] Mirolyubov EN, Kurtepov MM, Tomashov ND. Study of the corrosion and electrochemical behavior of stainless steels during cathodic polarization in nitric acid solutions. Bull Acad Sci USSR Div Chem Sci 1960;9:949–54. https://doi.org/10.1007/BF00903967.
[48] Whillock GOH, Worthington SE. Corrosion in nitric acid. In: Shreir's corros. Elsevier; 2010. p. 1250–69. https://doi.org/10.1016/B978-044452787-5.00053-6.
[49] Asami K, Hashimoto K, Shimodaira S. An XPS study of the passivity of a series of iron—chromium alloys in sulphuric acid. Corros Sci 1978;18:151–60. https://doi.org/10.1016/S0010-938X(78)80085-7.
[50] Maji BC, Das CM, Krishnan M, Ray RK. The corrosion behaviour of Fe-15Mn-7Si-9Cr-5Ni shape memory alloy. Corros Sci 2006;48:937–49. https://doi.org/10.1016/j.corsci.2005.02.024.
[51] Moriya Y, Kimura H, Ishizaki S, Hashizume S, Suzuki S, Suzuki H, Sampei T. Properties of Fe-Cr-Ni-Mn-Si (-Co) shape memory alloys. J Phys IV 1991;1:433–7. https://doi.org/10.1051/jp4:1991465.
[52] Alvarez SM, Bautista A, Velasco F. Influence of strain-induced martensite in the anodic dissolution of austenitic stainless steels in acid medium. Corros Sci 2013;69:130–8. https://doi.org/10.1016/j.corsci.2012.11.033.
[53] Hahin C, Stoss RM, Nelson BH, Reucroft PJ. Effect of cold work on the corrosion resistance of nonsensitized austenitic stainless steels in nitric acid. Corrosion 1976;32:229–38. https://doi.org/10.5006/0010-9312-32.6.229.
[54] Park K, Kwon H. Effects of Mn on the localized corrosion behavior of Fe-18Cr alloys. Electrochim Acta 2010;55:3421–7. https://doi.org/10.1016/j.electacta.2010.01.006.
[55] Padhy N, Paul R, Kamachi Mudali U, Raj B. Morphological and compositional analysis of passive film on austenitic stainless steel in nitric acid medium. Appl Surf Sci 2011;257:5088–97. https://doi.org/10.1016/j.apsusc.2011.01.026.
[56] Maurice V, Yang WP, Marcus P. X-Ray photoelectron spectroscopy and scanning tunneling microscopy study of passive films formed on (100) Fe-18Cr-13Ni single-crystal surfaces. J Electrochem Soc 1998;145:909–20. https://doi.org/10.1149/1.1838366.
[57] Machet A, Galtayries A, Zanna S, Klein L, Maurice V, Jolivet P, Foucault M, Combrade P, Scott P, Marcus P. XPS and STM study of the growth and structure of passive films in high temperature water on a nickel-base alloy. Electrochim Acta 2004;49:3957–64. https://doi.org/10.1016/j.electacta.2004.04.032.

[58] Fredriksson W, Malmgren S, Gustafsson T, Gorgoi M, Edström K. Full depth profile of passive films on 316L stainless steel based on high resolution HAXPES in combination with ARXPS. Appl Surf Sci 2012;258:5790–7. https://doi.org/10.1016/j.apsusc.2012.02.099.

[59] Kajimura H, Usuki N, Nagano H. Dual layer corrosion protective film formed on Si bearing austenitic stainless steel in highly oxidizing nitric acid. In: Proceedings of the symposium on passivity and Its breakdown; 1998. p. 332–43.

[60] Hio K, Adachi T, Yamada T, Tsuchida Y, Nakajima K, Hosoi Y. Effects of Al, Si and Mo on passivation characteristics of Fe-10Cr alloys. Mater Trans 2001;42:1723–30. https://doi.org/10.2320/matertrans.42.1723.

[61] Ioka I, Mori J, Kato C, Futakawa M, Onuki K. Characterization of passive films on Fe-Si alloy in boiling sulfuric acid. J Mater Sci Lett 1999;18:1497–9. https://doi.org/10.1023/A:1006638216420.

[62] Armijo JS. Intergranular corrosion of nonsensitized austenitic stainless steels — I. Environmental variables. Corrosion 1965;21:235–44. https://doi.org/10.5006/0010-9312-21.7.235.

[63] Furuya T, Kawafuku J, Satoh H, Shimogori K, Aoshima A, Takeda S. A corrosion testing method for titanium in nitric acid environments. ISIJ Int 1991;31:189–93. https://doi.org/10.2355/isijinternational.31.189.

[64] Laurent B, Gruet N, Gwinner B, Miserque F, Rousseau K, Ogle K. The kinetics of transpassive dissolution chemistry of stainless steels in nitric acid: the impact of Si. Electrochim Acta 2017;258:653–61. https://doi.org/10.1016/j.electacta.2017.11.110.